ADVANCED MATERIALS
www.advmat.de

Nonvolatile Electric Control of Ferromagnetism in Van Der Waals Multiferroic Heterostructures at Room Temperature

Hanzhang Zhao, Chao Yang, Yadong Liu, Qiaoqiao Wang, Yongyi Wu, Qiuxuan Mu, Feiyan Hou, Tai Min, and Tao Li**

Multiferroic heterostructures offer a promising platform for next-generation low-power spintronic devices by enabling electric-field control of magnetism. While recent advances in two-dimensional (2D) van der Waals (vdW) magnetic and ferroelectric materials have sparked significant interest, achieving reliable and nonvolatile electrical modulation of magnetism at room temperature within vdW multiferroic heterostructures remains a substantial challenge. Here, this study demonstrates robust, reproducible, and nonvolatile electrical control of ferromagnetism in $Fe_3GaTe_2/CuInP_2S_6$ multiferroic heterostructures under ambient conditions. The modulation is evidenced macroscopically by reshaped magnetic hysteresis loops in anomalous Hall voltage measurements and microscopically by in situ magnetic and electric field-induced domain evolution captured via magnetic force microscopy. The first-principles calculations reveal that the polarization of $CuInP_2S_6$ induces a significant modulation of the Dzyaloshinskii-Moriya interaction (DMI) in Fe_3GaTe_2. Incorporating these effects into micromagnetic simulations reproduces key features of the experimental hysteresis behaviors, indicating that the polarization-enhanced DMI lowers domain wall formation energy and drives a transition from coherent to incoherent magnetic reversal. These findings not only surmount the challenge of electrically modulating ferromagnetism in vdW systems via remanent ferroelectric polarization at room temperature but also open new pathways for energy-efficient skyrmion manipulation and vdW spintronic device engineering.

1. Introduction

Single-phase multiferroic materials exhibiting two or more ferroic properties (typically from ferroelectricity, ferromagnetism, and ferroelasticity) represent a critical material system for developing multifunctional devices.[1] Much of the research has focused on magnetoelectric materials that exhibit ferroelectric and ferromagnetic behaviors simultaneously.[2] However, the inherent mutual exclusivity between magnetism and electric polarization makes single-phase multiferroics rare. Their relatively weak macroscopic magnetoelectric coupling limits their practical applications further.[3] To address these challenges, fabricating multiferroic heterostructures has become a promising approach, enabling electric-field control of magnetism and facilitating a comprehensive investigation of the interfacial interplay between magnetic and electric polarization orders.[4] With the advent of van der Waal (vdW) ferroelectric and ferromagnetic materials, the exploration of multiferroic heterostructures has expanded to vdW systems. Compared to classical three-dimensional material systems, vdW materials feature dangling-bond-free surfaces, which enable them to maintain stability at atomic-scale thickness without requiring lattice matching with underlying substrates.[5] Furthermore, due to their unique electronic structures, vdW materials exhibit quantum confinement effects,[6] offering potentially enhanced magnetoelectric coupling and discovering novel quantum phenomena, particularly in the field of spintronics.[7] Additionally, the assembly of vdW heterostructures does not require complex growth techniques or lattice matching, simplifying the manufacturing process and broadening design possibilities for heterostructures.[7a] Despite extensive theoretical studies on vdW multiferroic heterostructures,[8] experimental realization remains limited, especially for systems that can operate at ambient conditions.[9]

Recent experimental studies have demonstrated the potential of vdW multiferroic heterostructures for electric-field-controlled modulation of magnetism. Liang et al. achieved nonvolatile magnetic modulation in heterostructures of vdW $Cr_2Ge_2Te_6$ and ferroelectric polymer P(VDF-TrFE) at 4 K. They observed

H. Zhao, C. Yang, Y. Liu, Q. Wang, Y. Wu, Q. Mu, F. Hou, T. Min, T. Li
Centre for Spintronics and Quantum Systems
State Key Laboratory for Mechanical Behavior of Materials
School of Materials Science and Engineering
Xi'an Jiaotong University
Xi'an 710049, China
E-mail: tai.min@nju.edu.cn; taoli66@xjtu.edu.cn
T. Min
Solid State Microstructure National Key Lab and Collaborative Innovation Centre of Advanced Microstructures
Nanjing University
Nanjing 210093, China
T. Min
School of Materials Science and Intelligent Engineering
Nanjing University
Suzhou 215163, China

The ORCID identification number(s) for the author(s) of this article can be found under https://doi.org/10.1002/adma.202500534

DOI: 10.1002/adma.202500534

simultaneous tuning of magnetic coercivity and remnant magnetization in thin layer samples, emphasizing the importance of interfacial coupling.[9b] Eom et al. reported voltage-controlled magnetism in $Fe_{3-x}GeTe_2/In_2Se_3$ multiferroic heterostructures at 80 K, identifying an in-plane strain-mediated mechanism using Raman spectroscopy and density functional theory (DFT).[9c] Similarly, Wu et al. demonstrated a nonreciprocal and nonvolatile tuning of magnetic coercivity via ferroelectric polarization in the CrI_3/In_2Se_3 system at 10 K, achieving up to 82% modulation of the critical magnetic transition field with a small gate voltage (5 V).[9a] While these studies demonstrated the ability of electric fields-modulated magnetic properties in vdW multiferroic heterostructures, they are volatile and operated at cryogenic temperatures, emphasizing the need for further exploration of room-temperature vdW multiferroic systems using remanent ferroelectric polarization.

Among vdW ferromagnetic materials, Fe_3GaTe_2 (FGT) has emerged as a robust candidate for room-temperature applications, with a reported Curie temperature (T_c) between 350 and 380 K.[10] FGT exhibits strong perpendicular magnetic anisotropy,[11] efficient thermo-spin conversion,[10] and skyrmions formation,[12] making it a versatile platform for spintronic devices, such as vdW spin valves,[13] magnetic tunnel junctions,[14] and spin-orbit torque devices.[15] On the other hand, CIPS, an intriguing vdW ferroelectric material, offers unique ferroelectric properties, including giant negative piezoelectricity,[16] multiple intrinsic polarization states,[17] and stable polarization retention[18] with a T_c above room temperature (≈315 K).[19] Given the high T_c of FGT and strong ferroelectricity of CIPS at room temperature, constructing vdW heterostructures with these materials offers a promising avenue for investigating magnetoelectric coupling effects and exploring novel device designs.

Here, we demonstrate the modulation of magnetization in FGT through the remanent polarization of CIPS in CIPS/FGT vdW multiferroic heterostructures under ambient conditions. As the vertically applied poling voltage increases, the magnetic coercive field of the device progressively decreases, accompanied by deformation of the magnetic hysteresis loop measured via the macroscopic Hall effect. Furthermore, microscopic magnetic domain imaging using magnetic force microscopy (MFM) under thermal excitation and magnetic cycling reveals that CIPS film facilitates the formation of magnetic domain walls in FGT while impeding their motion, which effectively explains the observed electrical Hall measurements. These phenomena can be attributed to the CIPS polarization-enhanced Dzyaloshinskii-Moriya interaction (DMI) in FGT as probed by our first-principles calculations. Additional micromagnetic simulations by incorporating different DMI and magnetic anisotropy parameters reproduce the key features of the experimentally observed ferromagnetic hysteresis loops, indicating that the polarization-enhanced DMI lowers domain wall formation energy and drives a transition from coherent to incoherent magnetic reversal. The successful realization of vdW heterostructures with effective magnetoelectric coupling at room temperature paves the way for fundamental research and potential spintronic applications in nonvolatile memory and neuromorphic computing.

2. Results and Discussion

2.1. Thickness-Dependent Magnetism of FGT Films

We grew the FGT crystals via the flux method, the stoichiometry of which was identified to be $Fe_{2.91}Ga_{0.99}Te_2$ by energy-dispersive X-ray spectroscopy (EDS) (Figure S1, Supporting Information). The ferromagnetic phase transition behaviors of bulk FGT crystals were characterized and confirmed by a superconducting quantum interference device (SQUID) (Figure S2, Supporting Information). The T_c of bulk FGT material was determined to be 360.8 K through dM/dT analysis (Figure S2a, Supporting Information), and the coercive field of FGT measured in the out-of-plane orientation at room temperature and 2 K is ≈20 Oe and 1000 Oe, respectively (Figure S2b, Supporting Information). On the other hand, CIPS single crystals were grown using the chemical vapor transport (CVT) method. The ferroelectric properties of exfoliated CIPS films were verified by Piezoresponse Force Microscopy (PFM). The as-prepared CIPS film exhibits a multidomain state, and the domain size is on the scale of hundreds of nanometers (Figure S3a,b, Supporting Information). The polarization of CIPS can be reversed by applying an electric field via the PFM tip, evidenced by the well-defined butterfly amplitude loop and the 180° reversal of the phase loop (Figure S3c, Supporting Information), from which the coercive field is estimated to be 0.27 MV cm^{-1}, similar to the previous report of 0.30 MV cm^{-1}.[20] In addition, the current-voltage loop was measured on a vertical two-terminal device with a voltage sweeping rate of 1.4 V s^{-1}. The loop demonstrates a clockwise switching sequence, and the current peaks arise from the polarization switching current (Figure S3d, Supporting Information).[21]

Magnetic behavior of vdW materials usually strongly depends on the film thickness.[22] We fabricated FGT films with varied thicknesses ranging from 11 to 528 nm on SiO_2 substrates and investigated their intrinsic magnetic properties through microscopic MFM and macroscopic Hall measurements. All the samples are investigated in the as-exfoliated state at 293 K in ambient conditions. The magnetic domain structures of FGT are illustrated in **Figure 1a**. Thick samples show typical Labyrinth domains, but with the decrease in the sample thickness, the domain width increases and tends toward a single-domain state. According to Kittel's law, the magnetic domain width (W) is expected to increase linearly with the square root of film thickness ($d^{1/2}$). However, our findings reveal that the magnetic domain width of FGT exhibits three different regimes as a function of film thickness. A typical example of determining the domain width of FGT is demonstrated in Figure S4 (Supporting Information). When the thickness was below ≈24 nm, FGT demonstrated a nearly single-domain state (region I in Figure 1b). In the thickness range of 28–113 nm, we observed that the magnetic domain width decreased with increasing FGT layer thickness (region II). In contrast, beyond a critical thickness of ≈113 nm, the trend reversed, and the magnetic domain width began to increase with FGT layer thickness (region III). The scaling of domain width as a function of FGT thickness exceeding 100 nm has been reported to conform to Kittel's law, which agrees well with our observation in region III.[23] The evolution of magnetic domain width with film thickness in region II can be accurately described by

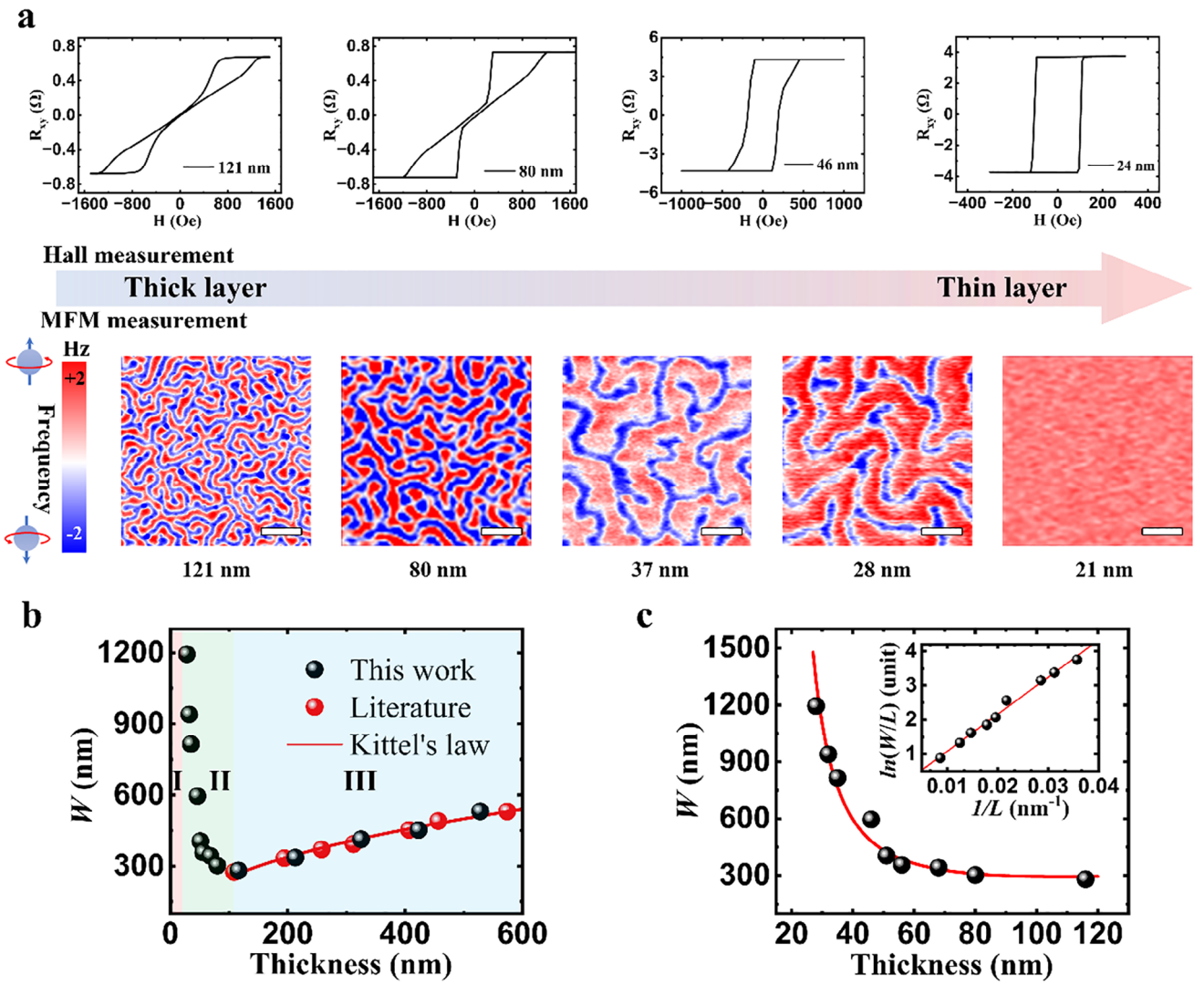

Figure 1. Thickness-dependent evolution of magnetic domain of pure FGT films. a) Thickness-dependent evolution of magnetic hysteresis loops and corresponding magnetic domain structures of FGT films. The scale bar represents 1 μm. b) Domain width W as a function of FGT thickness. The magnetic domain evolution can be divided into three regions (I: single-domain region, II: Kaplan's region, and III: Kittel's region). c) Fitting of domain width W as a function of FGT thickness according to Kaplan's law.

Kaplan's theory,[22] which refines Kittel's theory on the evolution of domain size in the thin-film region. According to Kaplan's law, the domain width W and the film thickness L obey the relation of $W = ALe^{\frac{\pi D_0}{2L}}$, where A is a constant, and D_0 is the dipolar length. The formula can be rewritten as:

$$ln\left(\frac{W}{L}\right) = \frac{\pi D_0}{2} \cdot \frac{1}{L} + lnA \quad (1)$$

By fitting with Equation (1), we obtain $D_0 = 68$ nm and $A = 1.04$. The fitting result is displayed in Figure 1c. The fitted constant A is close to the theoretical calculations by Kaplan[22] and Yafet[24] (0.955 and 1, respectively), confirming the experimental consistency with the theory. These findings not only fill the experiment gap of the sub-100 nm thickness-dependent domain evolution of FGT but also corroborate the validity of the continuum model employed within Kaplan's theoretical framework for vdW systems.

In addition, Hall measurements were conducted on the sub-100 nm samples to measure the magnetic hysteresis loops with varied FGT thickness. The extracted coercive field (H_c), saturation field (H_s), remanent Hall resistance (R_r), and saturation Hall resistance (R_s) as a function of the FGT flake thickness are depicted in Figure S5 (Supporting Information). The 121 nm sample exhibited soft magnetism behavior and nearly zero remanent magnetization, while the 80 nm sample showed an increase in remnant magnetization, which is the signature of gradual enhancement of perpendicular magnetic anisotropy.[25] The 46 nm and 24 nm samples had a square-like hysteresis loop, indicating a trend toward a coherent reversal and hard magnetic state. These Hall measurement results agree well with the

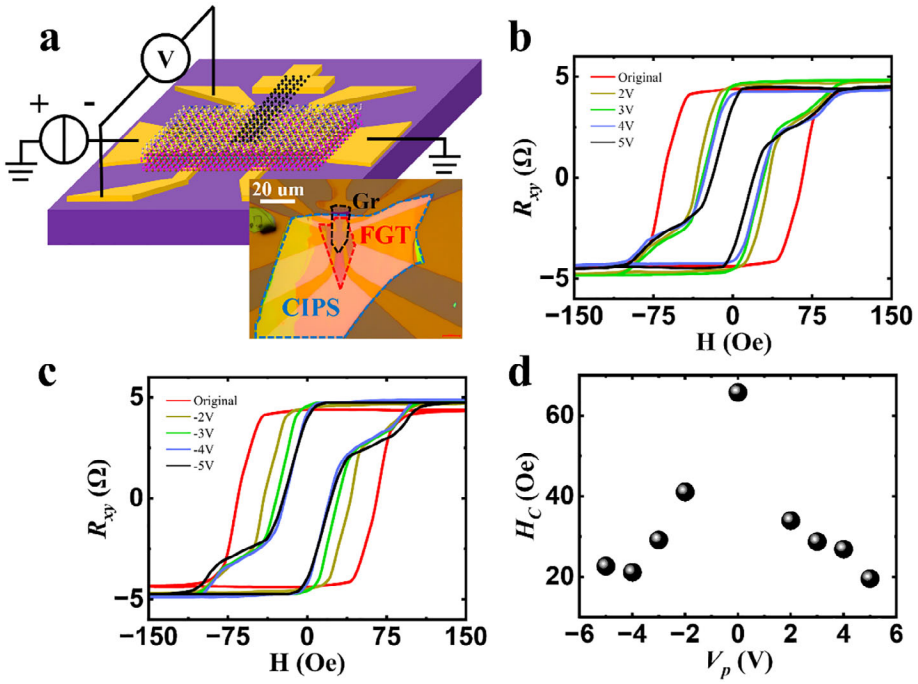

Figure 2. Hall measurements reveal nonvolatile modulation of the magnetic behavior of CIPS/FGT heterostructure at room temperature. a) Schematic of the heterostructure for Hall measurements. The thickness of CIPS and FGT are 80 nm and 14 nm, respectively. Inset is the optical image of the device. b) The Hall hysteresis loops of the CIPS/FGT device as a function of polarization voltage using positive V_p and c) negative V_p at room temperature. d) The magnetic coercive field plotted as a function of V_p.

thickness-dependent microscopic magnetic domain structures observed using MFM.

2.2. Modulation of Ferromagnetism with Remanent Polarization at Room Temperature

To achieve the electric control of the magnetic properties of FGT, we fabricated CIPS/FGT Hall devices by transferring CIPS/FGT heterostructure onto the pre-patterned electrode using the dry transfer technique.[26] The detailed sample fabrication process is described in the Experimental Methods. The optical image of the device and its schematic structure are illustrated in **Figure** 2a. The thickness of CIPS and FGT, as characterized by atomic force microscopy (AFM), were 80 nm and 14 nm, respectively. We first applied an external polarization voltage V_p between the graphite (Gr) top electrode and the Au/Ti bottom electrode to polarize CIPS. Subsequently, we stopped applying V_p and probed the magnetic properties of the heterostructure using Hall measurement to explore the modulation of the magnetic behavior of FGT by remanent polarization of CIPS at room temperature. The Hall hysteresis loop obtained from the multiferroic heterostructure in the pristine state exhibits a square shape. After applying a positive poling voltage V_p, the pristine hysteresis loop is highly distorted, accompanied by a large reduction of H_c. H_c is consistently reduced as the magnitude of V_p is increased (Figure 2b), while the same H_c reduction was observed by applying negative V_p (Figure 2c), which can be clearly visualized in Figure 2d, presenting a symmetric effect from opposite polarization states. Additionally, the tunability of H_c can be evaluated by the tuning range defined as the parameter $t = 1\text{-}\ H_{c\,min}/\ H_{c\,max}$.[9a] For $In_2Se_3/Fe_{2.64}GeTe_2$ device in ref,[9c] the tuning range t is 74% (at 80 K while applying gate voltage), and for our device, t is calculated to be 78% at room temperature, suggesting an efficient modulation effect. Another intriguing observation is that without applying a polarization voltage, the magnetic reversal process exhibited an abrupt transition, whereas, under the application of polarization voltage, the switching process became more gradual. This suggests a multidomain behavior that the polarization may significantly impact domain wall motion, warranting further investigation and verification. To demonstrate the repeatability of the experimental observations, we fabricated an additional device of the same structure but with a thicker FGT layer, which also demonstrated the decreased H_c with increased polarization voltage (Figure S6, Supporting Information). To further verify the role of the CIPS in the gate voltage (V_g)-induced changes in H_c, we conducted additional V_g-dependent Hall measurements using an h-BN (30 nm)/FGT (18 nm) heterostructure, replacing the CIPS by paraelectric and insulating h-BN. The hysteresis loops remain unaffected by the V_g up to ±10 V in h-BN/FGT heterostructure (Figure S7, Supporting Information), suggesting the critical role of CIPS in the effective tuning of the magnetic behavior of FGT.

2.3. Magnetic Domain Evolution of FGT Under the Influence of CIPS Polarization

To further investigate the coupling between vdW ferromagnetic and ferroelectric materials, we investigated the microscopic

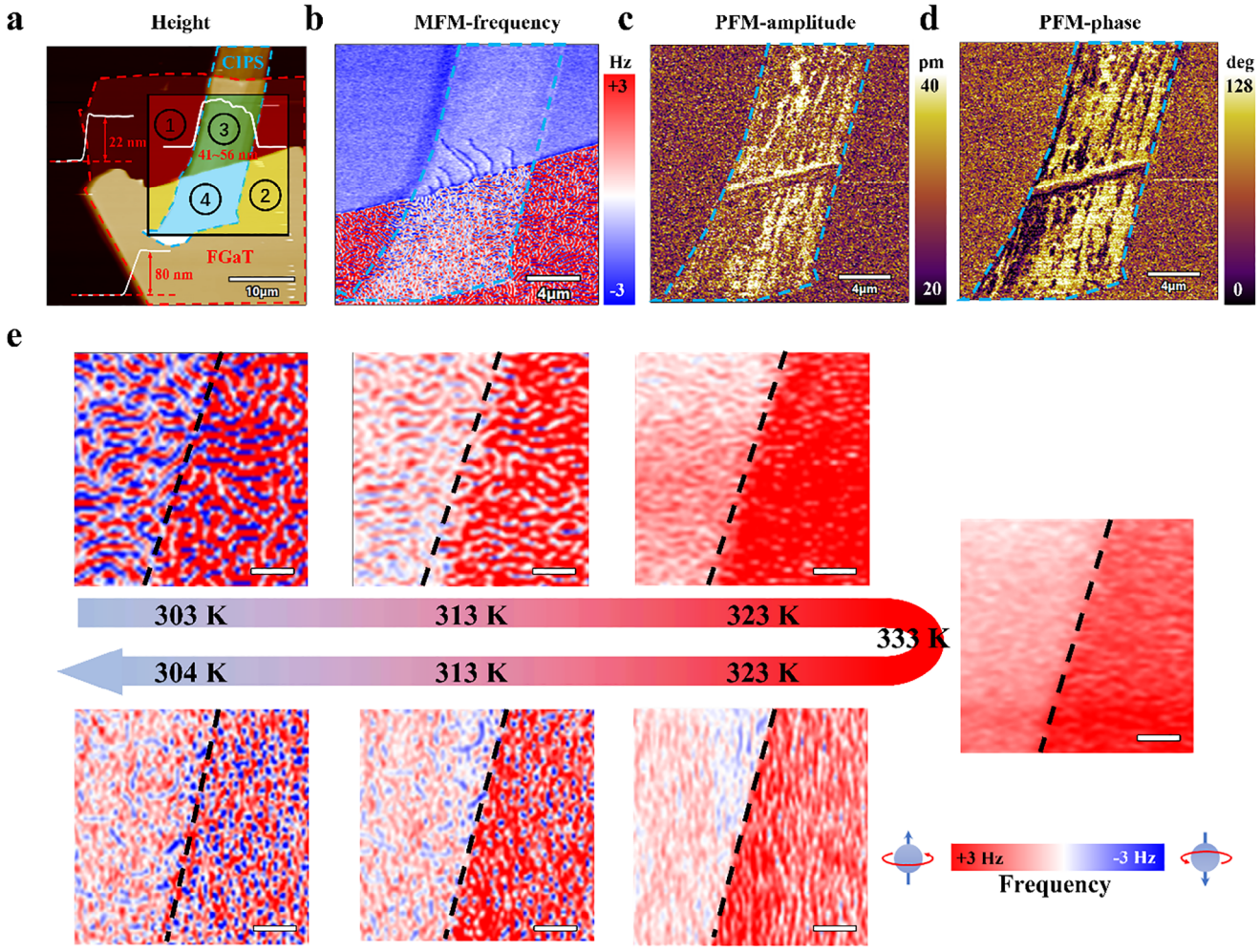

Figure 3. Magnetic domain evolution of CIPS/FGT heterostructure under thermal cycling. a) AFM image of the CIPS/FGT heterostructure and the thicknesses of CIPS and FGT were labeled. The boundaries of CIPS and FGT are outlined by blue and red dashed lines, respectively. b) MFM image of the as-prepared CIPS/FGT heterostructure. PFM amplitude c) and phase d) image of the as-prepared CIPS/FGT heterostructure. e) The corresponding MFM images of the CIPS/FGT heterostructure (on the left) and bare FGT (on the right) during in situ thermal cycling, within the scanned area indicated by the black square in (a). The scale bar represents 1 μm.

domain of the CIPS/FGT heterostructure using various scanning probe microscopy (SPM) techniques. The morphology of the heterostructure was characterized by AFM (**Figure** 3a), where the thickness of CIPS ranged from 41 to 56 nm and the FGT layer showed two distinct regions with thicknesses of 22 nm and 80 nm, respectively. The magnetic domain (Figure 3b) and the ferroelectric response (Figure 3c,d) of the as-prepared heterostructure were characterized by MFM and PFM, respectively. The PFM amplitude (Figure 3c) and phase (Figure 3d) only showed strong signals in the area of CIPS in the heterostructure, and demonstrated no correlation with the magnetic domain structure. Based on the different layer thicknesses and the overlap condition between CIPS and FGT, the sample is divided into four regions (four numbered regions in Figure 3a), including 1) 22 nm-thick bare FGT with uniform magnetic domain, 2) 80 nm-thick bare FGT with multidomain configuration, 3) CIPS-covered 22 nm-thick FGT, and 4) CIPS-covered 80 nm-thick FGT. To have a better spatial resolution of the magnetic domains, the scanning regions were confined in the area enclosed by the black square, and the regions 1 to 4 are highlighted with red, yellow, green, and blue colors (Figure 3a). Due to the farther separation between the MFM probe and the FGT layer, the observed MFM signal is generally weaker (reduced color contrast) in the CIPS-covered area (regions 3 and 4) than in the bare FGT surface (regions 1 and 2).

To systematically investigate the impact of CIPS on FGT, we conducted in situ magnetic field cycling and thermal excitation experiments. In regions 1 and 3, where FGT is relatively thin, both FGT and CIPS/FGT exhibit nearly uniform magnetic domain structure. To obtain a clear visualization of the domain evolution triggered by thermal excitation, we thus focused on the boundary between regions 2 and 4 (Figure 3e), which initially exhibited a Labyrinth multidomain pattern at 303 K. The magnetic domains are continuous across the boundary between these two regions, and the red shade domains appear weakened in the CIPS/FGT region. As the temperature increased to 313 K, the blue shade domains shrunk in both regions and the strength of

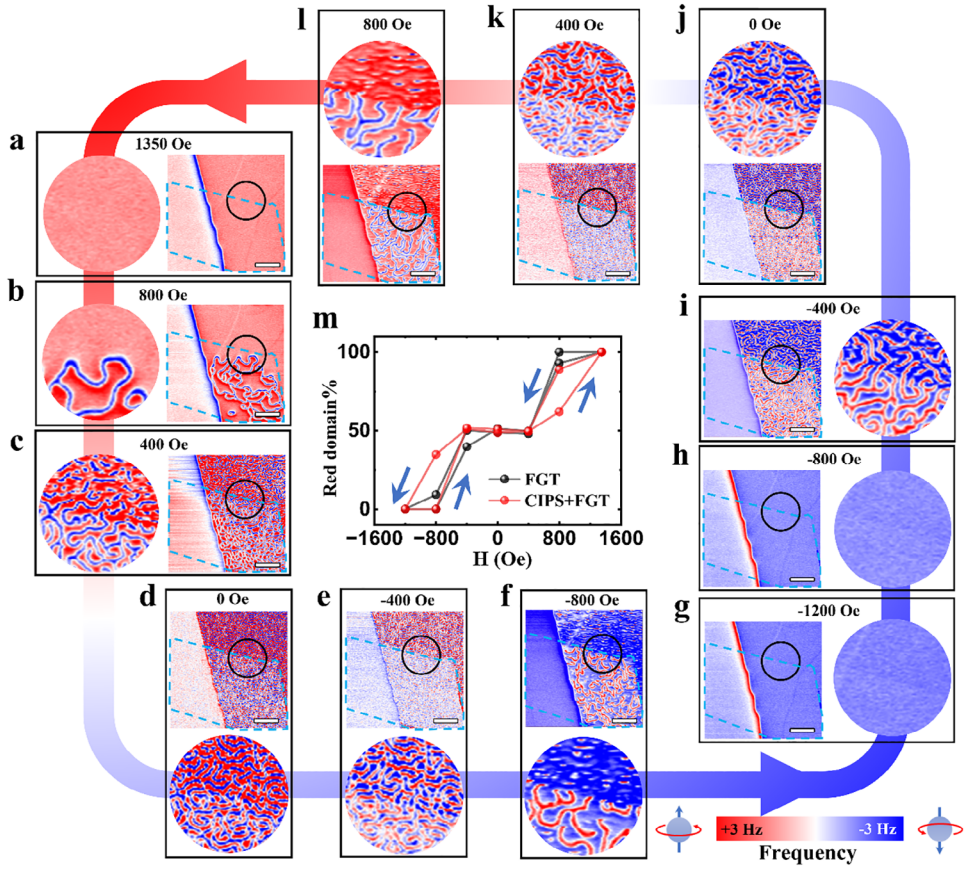

Figure 4. Magnetic domain evolution of CIPS/FGT heterostructure under magnetic cycling. a-l) MFM images of the CIPS/FGT heterostructure acquired during an applied magnetic field sweep. In each square image, the blue dashed lines outline the CIPS film region, the left and right sides of the image are the 22-nm-thick FGT and 80-nm-thick FGT regions, respectively. The scale bar represents 3 μm. The round images provide magnified views of the areas denoted by the black circles. m) Quantitative analysis of the magnetic domain area within regions 2 and 4 as a function of the magnetic field. The percentage of red domain area is calculated to track the evolution of the magnetic domain structure.

the MFM signal measured over the CIPS/FGT heterostructure was largely reduced. When the temperature is further increased to 323 K, the entire FGT area approaches a single domain state, but CIPS/FGT heterostructure still exhibits faint domain contrast, suggesting a potential increase in T_c of FGT in the heterostructure. At 333 K, the domain contrast becomes completely uniform in both regions, and the MFM signal strength is generally reduced, suggesting that the T_c of FGT is close to 333 K. During the cooling process, the domain structure starts to emerge at 323 K, but with distinct domain pattern compared to those during the heating process. When the temperature was reduced to room temperature (≈304 K), FGT flake (region 2) exhibited a bunch of newly formed circular blue domains spread in the red domains, which are absent in the as-prepared sample. In contrast, in the heterostructure area (region 4), mixed types of circular and stripe domains emerged with a largely reduced density of the circular domains. These newly emerged circular magnetic domains can potentially be the skyrmions, which have been reported to form after thermal cycling in FGT nanosheets.[12,27]

We also investigated the in situ magnetic domain evolution of the CIPS/FGT heterostructure through magnetic field cycling of regions 2 and 4 (**Figure 4**. The set values of the applied magnetic fields are labeled in each figure, while the real field values were calibrated using a gaussmeter, and their relationship can be found in Figure S8 (Supporting Information). Under an external out-of-plane magnetic field of 1350 Oe (Figure 4a), both regions 2 and 4 exhibit a single-domain state (red domain), indicating the saturation of the magnet moment in FGT. When the magnetic field was reduced to 800 Oe (Figure 4b), pure FGT (region 2) retained its single-domain configuration, while long belts of blue domains began to develop in the heterostructure (region 4). As the magnetic field was further reduced to 400 Oe (Figure 4c), multiple domains emerged and evolved into Labyrinthine domain structures in region 2. In contrast, large patches of red domains appeared in the heterostructure region 4. When the magnetic field was lowered to 0 Oe (Figure 4d), the domain width decreased, and the domain pattern of regions 2 and 4 began to converge, but with more area of weak response (white color) in the heterostructure region. When the magnetic field direction was reversed to −400 Oe (Figure 4e), the red domain area was reduced, and the domain walls (represented by the white color) in both areas widened considerably. As the magnitude of the magnetic field was further increased to −800 Oe (Figure 4f), long belts of red domains were formed in region 4, while in region 2, nearly a uniform blue domain was formed that intercalated with a few circular red domains. Finally, when the magnetic field reached

−1200 Oe (Figure 4g), the domain walls in both regions completely disappeared, indicating a fully reversed and saturated domain state. In the other half cycle, from the negatively saturated state to the positively saturated state, the domain evolution follows a similar trend as that depicted from Figure 4a–g sequentially. We noted the different domain structures evolved under the same magnetic field strength in opposite polarity (±800 Oe), as illustrated in Figure 4b,h, which can be ascribed to the drift of the magnetic field. The specific discussion is included in Note S1 (Supporting Information). The percentages of the red magnetic domain area in regions 2 and 4 as a function of the magnetic field are plotted in Figure 4m. The evolution of the magnetic domain proportion in region 4 exhibits a more pronounced hysteresis effect compared to that in region 2, suggesting that CIPS facilitates the formation of magnetic domain walls and hinders their further motion.

To clearly demonstrate the magnetoelectric coupling in the heterostructure, we conducted in situ voltage-controlled magnetic domain measurements on an FGT/CIPS heterostructure. The FGT magnetic domain in the heterostructure was saturated first by applying a magnetic field of 1000 Oe. The external magnetic field was then reduced to 0 Oe, confirming that the remanent state remained saturated. We applied a +8 V tip bias (larger than the coercive bias of CIPS verified by PFM) to the CIPS layer by scanning the entire heterostructure surface. The magnetic domain of FGT was observed under the remanent state of CIPS. The applied electric bias resulted in the emergence of a small fraction of the magnetic domain in the belt shape (Figure S10a, Supporting Information), similar to that observed in Figure 4b. The effect of the negative tip bias was investigated in the same way, which induced a similar partial magnetic domain reversal in the same direction (Figure S10b, Supporting Information). Furthermore, we create a multidomain state of FGT as the initial state via appropriate external magnetic fields before applying an electric bias. Then, +8 V tip bias was applied again, which further increased the reversed domain area and domain wall density (Figure S10c, Supporting Information). These findings substantiate that electric bias can effectively induce magnetic domain reversal, and the positive and negative electric biases result in the same direction of magnetic domain, consistent with the symmetric polarization effect on H_c obtained in the Hall measurements (Figure 2d).

2.4. Mechanism of the Magnetoelectric Coupling

We performed first-principles calculations to investigate the effect of opposite ferroelectric polarization states (P_{up} and P_{down}) of CIPS on the magnetization of FGT in the multiferroic heterostructure, where $\sqrt{3}\times\sqrt{3}\times 1$ FGT and 1×1×1 CIPS were utilized to ensure lattice match. **Figure 5a** presents the band structure of freestanding FGT as a reference, while Figure 5b depicts the band structures of the FGT/CIPS heterostructure under the P_{up} and P_{down} states of CIPS. The comparison indicates that the band structure of FGT remains unchanged upon forming the heterostructure, suggesting minimal orbital hybridization at the interface due to the weak vdW interaction. However, the FGT bands exhibit a small upward energy shift attributed to a modified chemical potential. Although polarization reversal of CIPS has little effect on the FGT band structure, it shifts the CIPS bands to lower energies due to the polarization-induced field effect. Figure 5c depicts the charge transfer at the CIPS/FGT interface under distinct ferroelectric polarization states, demonstrating that the dominant charge redistribution occurs between S and Te atoms. The electron depletion in the bottom-layer Te atoms induces an asymmetric charge transfer in the Fe_{II} sites in FGT, indicating symmetry breaking. The magnetic parameters, including the average magnetic moments of the Fe atoms, magnetic anisotropy energy (MAE), and DMI coefficient (D), with respect to opposite CIPS polarization states, are plotted in Figure 2d. The calculation details are described in Note S2 (Supporting Information). Compared with the freestanding FGT, in FGT/CIPS heterostructure, the magnetic moment of the top Fe_I (2.35 μ_B) and bottom Fe_I (2.29 μ_B) atoms (depicted by the black arrow in Figure 5c) become no longer equivalent, again indicating the inversion symmetry breaking of FGT.[28] The inversion symmetry breaking in a magnetic system can lead to DMI,[29] which plays an important role in understanding chiral magnetic structures.[30] In our modeled CIPS/FGT heterostructure, a large DMI is introduced compared to the freestanding FGT, which weakly depends on the CIPS polarization direction. Additionally, the interfacial effect in CIPS/FGT results in enhanced MAE, the strength of which is larger under the upward polarization direction of CIPS.

To verify the effect of emergent large DMI on the magnetism of FGT, we conducted micromagnetic modeling to acquire the hysteresis loop and domain evolution of FGT with varied DMI coefficient D, while the rest parameters were adopted from literature (see "Experimental Methods" for detail). We found that with the increment of D, the hysteresis loop changes from a coherent reversal to an incoherent reversal pattern. The incoherent reversal is associated with multidomain formation (Figure S13, Supporting Information), the process of which starts from the nucleation of the Labyrinth domain wall at a small magnetic field range, following domain wall motion that requires a larger magnetic field to saturate the sample than the coherent reversal type. Figure 5e illustrates the comparison between the simulated and experimentally observed hysteresis loops, demonstrating good consistency. We also analyzed the energy changes associated with the hysteresis loop and determined that DMI reduces the total energy of the system primarily by lowering the exchange energy. This reduction originates from DMI and stabilizes Néel-type domain walls, as elaborated in Note S3 (Supporting Information).

An unexpected observation is the symmetric electric bias modulation in the Hall measurement, independent of the remanent polarization direction of CIPS. This can be explained by the competing effects from DMI and the uniaxial anisotropy constant K_u (corresponding to MAE in first-principles calculations, where K_u is proportional to MAE). Figure 5f shows the 2D map of the extracted coercive fields as a function of D and K_u. The increased K_u or the decreased magnitude of D can both result in a higher coercive field, indicating the competing relationship between DMI and magnetic anisotropy, which agrees with reported magnetic models.[31] Figure 5g shows four characteristic hysteresis loops labeled with numbers 1 to 4, corresponding to those labeled in Figure 5f. In the FGT/CIPS heterostructure, when CIPS polarization points to FGT (P_{up}), the magnitude of both K_u and D are larger than those when CIPS

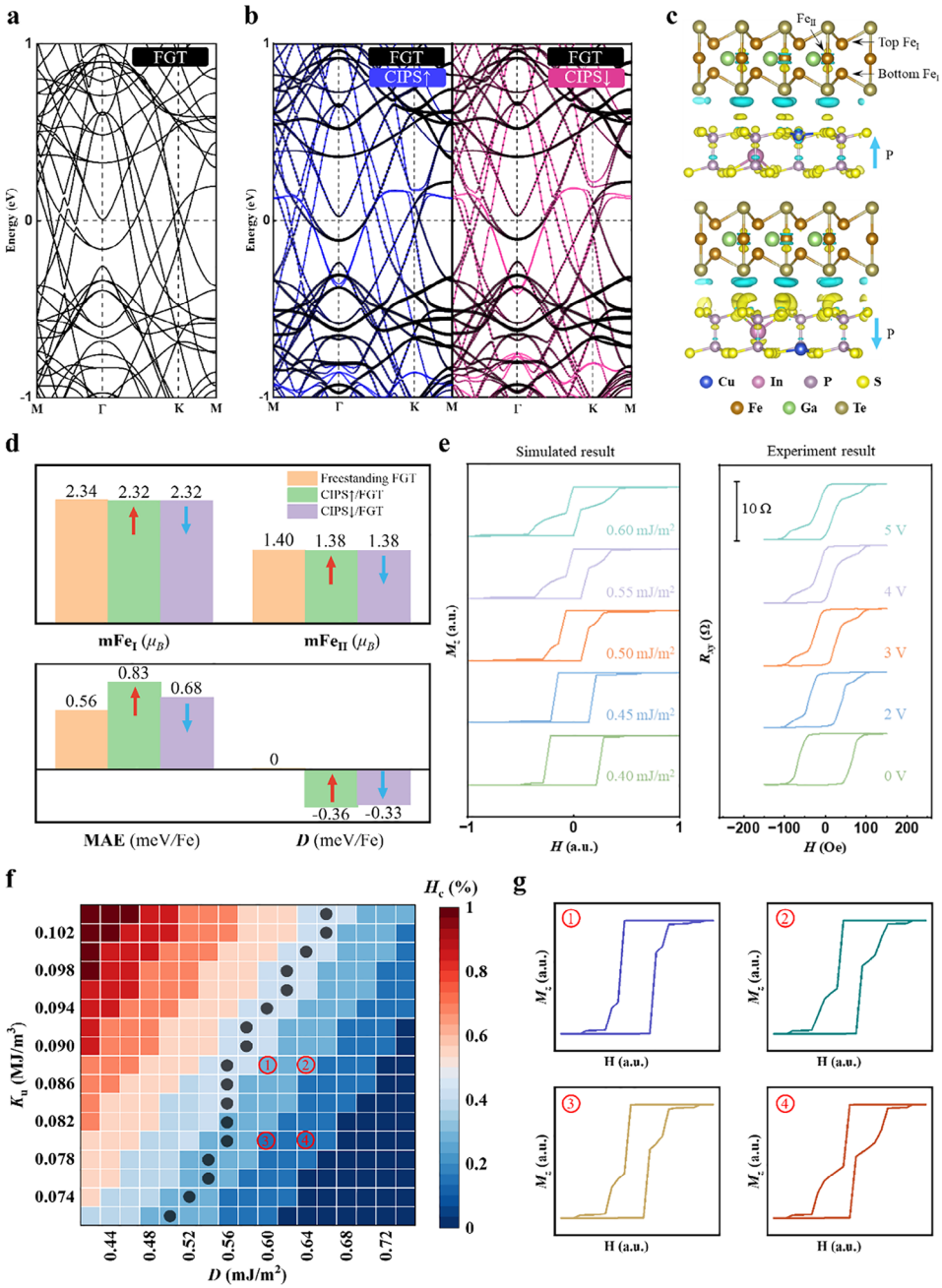

Figure 5. First-principles calculations and micromagnetic modeling reveal the mechanism of the magnetoelectric coupling in FGT/CIPS multiferroic heterostructure. a) Band structure of a freestanding FGT monolayer. b) Band structure of the FGT/CIPS heterostructure with upward (left) and downward (right) polarization directions of CIPS. c) Charge transfer near the heterostructure interface (isosurface = 0.001 e/Bohr^3) with upward and downward polarization states of CIPS. d) Magnetic parameters, including the magnetic moment of Fe ions, MAE, and DMI coefficient D, of FGT/CIPS heterostructure under opposite polarization states of CIPS and freestanding FGT. e). Comparison between the simulated hysteresis loops (with varied D) and experimentally observed loops (under varied polarization voltage). f) 2D map of the simulated coercive fields as a function of K_u and D. The black dots indicate the threshold at which the reversal pattern transitions from coherent to incoherent behavior. g) Simulated hysteresis loops corresponding to the combination of D and K_u labeled as ①–④ in (f).

polarization is pointing away from FGT (P_{down}). Thus, the relative relationship between FGT (P_{up}) and FGT (P_{down}) corresponds to the hysteresis loop ② and ③, respectively, demonstrating similar shapes of loops. Additionally, to investigate the potential role of interfacial stress in the FGT/CIPS heterostructure, we performed Raman spectroscopy measurements. The obtained spectra revealed no significant stress-related peak shifts, indicating negligible interfacial stress under the examined conditions. The specific results and analysis are shown in Note S4 (Supporting Information).

3. Conclusion

In this work, we successfully realized robust nonvolatile electric control of magnetism at room temperature in $Fe_{2.91}Ga_{0.99}Te_2/CuInP_2S_6$ multiferroic heterostructures. Hall measurements revealed a transition in the magnetic reversal pattern from coherent to incoherent behavior as a function of polarization voltage. The MFM results provided direct observations of microscopic domain evolution, demonstrating that CIPS promotes domain wall nucleation while impeding their motion. Combining first-principles calculations with micromagnetic simulations, we found that CIPS induces inversion symmetry breaking in FGT that significantly enhances its DMI, with the DMI strength depending on the CIPS polarization directions. This enhanced DMI reduces the exchange energy in the system, thereby facilitating domain wall formation but hindering its motion. This work represents a significant step forward in the practical application of vdW multiferroic materials and establishes a promising platform for future research on skyrmion manipulation.

4. Experimental Section

Crystal Growth of FGT: High-quality $Fe_{2.91}Ga_{0.99}Te_2$ single crystals were grown using a self-flux method. High-purity Fe powders (Aladdin, 99.95%), Ga lumps (Aladdin, 99.99999%), and Te powders (Aladdin, 99.99%) in the molar ratio of 1:1:2 were placed in an evacuated quartz tube and sealed (vacuum at the level of $\approx 10^{-3}$ Pa). The mixture was first heated to 1000 °C within 1 h and held at this temperature for 24 h to allow solid reactions. The temperature was rapidly decreased to 880 °C over 1 h followed by a slow cooling to 780 °C over 100 h.

Crystal Growth of CIPS: Single crystalline CIPS crystals were synthesized using the CVT method. The powders of Cu (Macklin, 99.80%), In (Macklin, 99.99%), P (Macklin, 98.90%), and S (Macklin, 99.90%) were encapsulated in a vacuum quartz tube (vacuum at the level of$\approx 10^{-3}$ Pa) according to stoichiometric ratios, and I_2 was used as the transport agent at a dosage of 2 mg cm^{-3}. The temperatures of the feedstock zone and the crystal growth zone were kept at 750 and 650 °C, respectively. After 7 days of reaction under these conditions, followed by a natural cooling process, greenish-yellow crystals were obtained.

Compositional Characterization of FGT: The crystals were mechanically exfoliated using conductive carbon adhesive tape to ensure a clean and flat surface for scanning electron microscopy (SEM, JEOL JSM-7000F, Jeol) measurements. The corresponding atomic percentages were obtained via EDS (INCA Energy System, Oxford).

Heterostructure Transfer Method: The FGT/CIPS heterostructures for MFM characterization were fabricated in the following. Bulk FGT crystals were mechanically exfoliated onto a silicon substrate using Scotch tape. Similarly, bulk CIPS crystals were exfoliated onto a polydimethylsiloxane (PDMS)-coated glass slide. Optical microscopy was utilized to identify and characterize the resulting flakes. The heterostructure was assembled using a 2D transfer platform through the following sequence: 1) The FGT/Si substrate was secured on the sample stage; 2) The PDMS/glass slide bearing CIPS was mounted onto an overhead cantilever assembly; 3) Micron-scale alignment between CIPS and FGT flakes was achieved via real-time optical monitoring; 4) A motor-controlled vertical approach facilitated interfacial contact; and 5) The PDMS substrate was slowly retracted to transfer CIPS onto the FGT/Si substrate. All steps were performed in an argon-filled glove box with H_2O and O_2 levels below 0.1 ppm. For devices intended for electrical characterization, the fabrication process entailed: 1) Exfoliation of CIPS, FGT, and graphene flakes onto PDMS-coated substrates using consistent exfoliation parameters; 2) Sequential transfer of FGT, CIPS, and graphene layers onto pre-patterned electrodes using the 2D transfer system; and 3) Thermal annealing under optimized conditions to improve the electrode-contact interface quality.

Device Fabrication and Hall Measurements: A standard Hall bar electrode of Ti/Au (3/7 nm) was pre-fabricated on a 285 nm SiO_2/Si substrate using a sequence of techniques: photolithography (Mask Aligner, MA6, Karl Süss), e-beam evaporation (Versatile Sputtering, Electron Beam, & Thermal Evaporation Deposition Platform, PVD75, Kurt J. Lesker), followed by lift-off. Mechanically exfoliated vdW materials were transferred onto the Hall bar pattern using the polydimethylsiloxane (PDMS) stamp in a glove box. The Hall measurement used a current source (Model 6221, Keithley) and a voltmeter (Model 2182A, Keithley) on a homemade probe station with an electromagnet. A source and measurement unit (Model 4200, Keithley) was employed to apply polarization voltages.

MFM Measurements: FGT samples with different thicknesses were exfoliated to the silicon substrate and measured at room temperature (except for thermal cycling). The magnetic domain measurements were performed with an atomic force microscope (MFP-3D Infinity, Oxford Instruments) using A Co/Cr coated tip (MFM-R2 Asylum Research). In MFM, the magnetic stray field from exfoliated FGT nanosheets was detected by a scanning nanoscale magnetic tip, allowing for imaging of the magnetic domain structures. Thermal and magnetic cycling were conducted using a heater module and a variable field module, respectively. In MFM, the coercive field of the MFM tip, which falls within 200–300 Oe, plays a crucial role. When the applied magnetic field during magnetic cycling exceeds this threshold, the magnetization of the MFM tip could reverse. This reversal leads to an inversion in the MFM imaging results. To accurately interpret the MFM results, the data corresponding to the reversed field of the MFM tip must be processed accordingly. This implies that features originally appearing as attractive forces (red regions) will now appear as repulsive forces (blue regions), and vice versa.

SQUID Measurements: The magnetism measurements were conducted in a commercial magnetic property measurement system (MPMS-squid VSM-094). A piece of FGT single crystal was cut into a disc shape and mounted on the sample holders. For *M-T* curves, the rate of temperature change was set to 2 K·min^{-1} with the interval of 1 K. For *M-H* curves, the rate of magnetic field change was set as 100 Oe s^{-1} with an interval of 400 Oe. Each point was measured after the temperature and magnetic field were stabilized to guarantee the accuracy of the result in both *M-T* and *M-H* curves.

Micromagnetic Simulation: Micromagnetic simulations were carried out using the GPU accelerated micromagnetic simulation program Mumax3.[32] The slab geometries of dimensions were 512×512×8 with a mesh size of 2×2×1.75nm. The total energy of the micromagnetic model contained exchange energy (including contributions from DMI and Heisenberg exchange interaction), anisotropy energy, magnetostatic energy, and Zeeman energy. The simulation parameters were adopted (exchange stiffness $A_{ex} = 1.3$ pJ m^{-1} and saturation magnetization $M_s = 2.5 \times 10^5$A m^{-1}) from literature,[12,33] which was determined by experiment and utilized for micromagnetic simulations of FGT. As indicated by the first-principles calculations result, CIPS results in varied DMI coefficient D and uniaxial magnetic anisotropy constant K_u in FGT. The D was varied in micromagnetic simulation and observed their effect on the magnetic reversal process. The varied DMI (K_u) was in the range of 0.40–0.74 mJ m^{-2} (0.072–0.104 MJ m^{-3}), which were reasonable values reported for FGT in literature (0–1.07 and 0.07–0.3 MJ m^{-3}).[12,33]

First-Principles Calculations: Our first-principles calculations were performed within the density functional theory formalism, and the calculation software package was the Vienna Ab-initio Simulation Package (VASP).[34] The projector-augmented wave (PAW)[35] method was employed to model the ionic potentials. The exchange and correlation energy was treated with the Perdew–Burke-Ernzerhof (PBE)[36] realization of the generalized gradient approximation (GGA).[37] Hubbard U was not employed for Fe 3d orbitals correction, referring to the previous studies.[33a,38] The energy cutoff was set to 400 eV, and a vacuum region larger than 15 Å was introduced to avoid interactions between neighboring layers. The vdW correction was considered by the DFT-D3 approach.[39] All the atoms were allowed to relax until the calculated forces converged to 0.01 eV $Å^{-1}$, and the energy precision was set to be 10^{-5} eV. The k-point grid of heterostructure

supercell 8 × 8 × 1 in the Monkhorst-Pack[40] scheme was used to sample the Brillouin zone for relaxation and self-consistent calculations. The spin-orbit coupling (SOC)[41] effect was taken into consideration for MAE and DMI calculations.

Supporting Information

Supporting Information is available from the Wiley Online Library or from the author.

Acknowledgements

This work was financially supported by the National Key R&D Program of China (Grants No. 2021YFA1202200, 2022YFB4400200) The authors would like to thank Ms. Xue Zhou at the Centre for Spintronics and Quantum Systems of Xi'an Jiaotong University for her assistance with magnetic dynamic analysis.

Conflict of Interest

The authors declare no conflict of interest.

Data Availability Statement

The data that support the findings of this study are available from the corresponding author upon reasonable request.

Keywords

$CuInP_2S_6$, electrical control of magnetism, Fe_3GaTe_2, spintronic devices, vdW multiferroic heterostructure

Received: January 8, 2025
Revised: May 14, 2025
Published online:

[1] a) M. M. Vopson, *Crit. Rev. Solid State Mater. Sci.* **2015**, *40*, 223; b) H. Schmid, *Ferroelectrics* **1994**, *162*, 317.
[2] a) W. Eerenstein, N. D. Mathur, J. F. Scott, *Nature* **2006**, *442*, 759; b) M. Fiebig, T. Lottermoser, D. Meier, M. Trassin, *Nat. Rev. Mater.* **2016**, *1*, 16046; c) J. Ma, J. Hu, Z. Li, C. W. Nan, *Adv. Mater.* **2011**, *23*, 1062.
[3] a) C. Lu, M. Wu, L. Lin, J.-M. Liu, *Natl. Sci. Rev.* **2019**, *6*, 653; b) C. A. F. Vaz, *J. Phys.: Condens. Matter* **2012**, *24*, 333201; c) M. Kumar, S. Shankar, A. Kumar, A. Anshul, M. Jayasimhadri, O. P. Thakur, *J. Mater. Sci.: Mater. Electron.* **2020**, *31*, 19487; d) R. Gupta, R. K. Kotnala, *J. Mater. Sci.* **2022**, *57*, 12710.
[4] a) K. Cai, M. Yang, H. Ju, S. Wang, Y. Ji, B. Li, K. W. Edmonds, Y. Sheng, B. Zhang, N. Zhang, S. Liu, H. Zheng, K. Wang, *Nat. Mater.* **2017**, *16*, 712; b) S. Lai, H. Liu, Z. Zhang, J. Zhao, X. Feng, N. Wang, C. Tang, Y. Liu, K. S. Novoselov, S. A. Yang, W.-b. Gao, *Nat. Nanotechnol.* **2021**, *16*, 869; c) J. M. Hu, L. Q. Chen, C. W. Nan, *Adv. Mater.* **2015**, *28*, 15; d) J. T. Heron, M. Trassin, K. Ashraf, M. Gajek, Q. He, S. Y. Yang, D. E. Nikonov, Y. H. Chu, S. Salahuddin, R. Ramesh, *Phys. Rev. Lett.* **2011**, *107*, 217202; e) Y. Wang, L. Wang, J. Xia, Z. Lai, G. Tian, X. Zhang, Z. Hou, X. Gao, W. Mi, C. Feng, M. Zeng, G. Zhou, G. Yu, G. Wu, Y. Zhou, W. Wang, X.-x. Zhang, J. Liu, *Nat. Commun.* **2020**, *11*, 3577.
[5] R. Ramesh, N. A. Spaldin, *Nat. Rev. Mater.* **2007**, *6*, 21.
[6] Y. Yi, Z. Chen, X. F. Yu, Z. K. Zhou, J. Li, *Adv. Quantum Technol.* **2019**, *2*, 1800111.
[7] a) K. S. Novoselov, A. Mishchenko, A. Carvalho, A. H. Castro Neto, *Science* **2016**, *353*, aac9439; b) J. F. Sierra, J. Fabian, R. K. Kawakami, S. Roche, S. O. Valenzuela, *Nat. Nanotechnol.* **2021**, *16*, 856.
[8] a) Y. Lu, R. Fei, X. Lu, L. Zhu, L. Wang, L. Yang, *ACS Appl. Mater. Interfaces* **2020**, *12*, 6243; b) B. Yang, B. Shao, J. Wang, Y. Li, C. Yam, S. Zhang, B. Huang, *Phys. Rev. B.* **2021**, *103*, L201405; c) Y. Zhao, J. J. Zhang, S. Yuan, Z. Chen, *Adv. Funct. Mater.* **2019**, *29*, 1901420; d) K. Dolui, M. D. Petrović, K. Zollner, P. Plecháč, J. Fabian, B. K. Nikolić, *Nano Lett.* **2020**, *20*, 2288; e) H.-X. Cheng, J. Zhou, C. Wang, W. Ji, Y.-N. Zhang, *Phys. Rev. B.* **2021**, *104*, 064443; f) W. Sun, W. Wang, H. Li, G. Zhang, D. Chen, J. Wang, Z. Cheng, *Nat. Commun.* **2020**, *11*, 5930; g) B. Wang, Y. Bai, C. Wang, S. Liu, S. Yao, Y. Jia, J. Cho, *Phys. Rev. B.* **2024**, *110*, 094423; h) X. Zhang, Z. Zhou, X. Yu, Y. Guo, Y. Chen, J. Wang, *Adv. Funct. Mater.* **2023**, *33*, 2301353; i) Q. Cui, Y. Zhu, J. Jiang, J. Liang, D. Yu, P. Cui, H. Yang, *Phys. Rev. Res.* **2021**, *3*, 043011; j) C. Gong, E. M. Kim, Y. Wang, G. Lee, X. Zhang, *Nat. Commun.* **2019**, *10*, 2657.
[9] a) Y. Wu, D. Zhang, Y. N. Zhang, L. Deng, B. Peng, *Nano Lett.* **2024**, *24*, 5929; b) S. Liang, T. Xie, N. A. Blumenschein, T. Zhou, T. Ersevim, Z. Song, J. Liang, M. A. Susner, B. S. Conner, S.-J. Gong, J.-P. Wang, M. Ouyang, I. Zutic´, A. L. Friedman, X. Zhang, C. Gong, *Nat. Electron.* **2023**, *6*, 199; c) J. Eom, I. H. Lee, J. Y. Kee, M. Cho, J. Seo, H. Suh, H. J. Choi, Y. Sim, S. Chen, H. J. Chang, S. H. Baek, C. Petrovic, H. Ryu, C. Jang, Y. D. Kim, C. H. Yang, M. J. Seong, J. H. Lee, S. Y. Park, J. W. Choi, *Nat. Commun.* **2023**, *14*, 5605.
[10] S. Liu, S. Hu, X. Cui, T. Kimura, *Adv. Mater.* **2023**, *36*, 2309776.
[11] G. Zhang, F. Guo, H. Wu, X. Wen, L. Yang, W. Jin, W. Zhang, H. Chang, *Nat. Commun.* **2022**, *13*, 5067.
[12] Z. Li, H. Zhang, G. Li, J. Guo, Q. Wang, Y. Deng, Y. Hu, X. Hu, C. Liu, M. Qin, X. Shen, R. Yu, X. Gao, Z. Liao, J. Liu, Z. Hou, Y. Zhu, X. Fu, *Nat. Commun.* **2024**, *15*, 1017.
[13] H. Pan, C. Zhang, J. Shi, X. Hu, N. Wang, L. An, R. Duan, P. Deb, Z. Liu, W. Gao, *ACS Mater. Lett.* **2023**, *5*, 2226.
[14] W. Jin, G. Zhang, H. Wu, L. Yang, W. Zhang, H. Chang, *ACS Appl. Mater. Interfaces* **2023**, *15*, 36519.
[15] S. N. Kajale, T. Nguyen, C. A. Chao, D. C. Bono, A. Boonkird, M. Li, D. Sarkar, *Nat. Commun.* **2024**, *15*, 1485.
[16] L. You, Y. Zhang, S. Zhou, A. Chaturvedi, S. A. Morris, F. Liu, L. Chang, D. Ichinose, H. Funakubo, W. Hu, T. Wu, Z. Liu, S. Dong, J. Wang, *Sci. Adv.* **2019**, *5*, aav3780.
[17] a) J. A. Brehm, S. M. Neumayer, L. Tao, A. O'Hara, M. Chyasnavichus, M. A. Susner, M. A. McGuire, S. V. Kalinin, S. Jesse, P. Ganesh, S. T. Pantelides, P. Maksymovych, N. Balke, *Nat. Mater.* **2019**, *19*, 43; b) T. Li, Y. Wu, G. Yu, S. Li, Y. Ren, Y. Liu, J. Liu, H. Feng, Y. Deng, M. Chen, Z. Zhang, T. Min, *Nat. Commun.* **2024**, *15*, 2653.
[18] S. Zhou, L. You, A. Chaturvedi, S. A. Morris, J. S. Herrin, N. Zhang, A. Abdelsamie, Y. Hu, J. Chen, Y. Zhou, S. Dong, J. Wang, *Mater. Horiz.* **2020**, *7*, 263.
[19] F. Liu, L. You, K. L. Seyler, X. Li, P. Yu, J. Lin, X. Wang, J. Zhou, H. Wang, H. He, S. T. Pantelides, W. Zhou, P. Sharma, X. Xu, P. M. Ajayan, J. Wang, Z. Liu, *Nat. Commun.* **2016**, *7*, 12357.
[20] X. Wang, C. Zhu, Y. Deng, R. Duan, J. Chen, Q. Zeng, J. Zhou, Q. Fu, L. You, S. Liu, J. H. Edgar, P. Yu, Z. Liu, *Nat. Commun.* **2021**, *12*, 1109.
[21] A. Chen, W. Zhang, L. R. Dedon, D. Chen, F. Khatkhatay, J. L. MacManus-Driscoll, H. Wang, D. Yarotski, J. Chen, X. Gao, L. W. Martin, A. Roelofs, Q. Jia, *Adv. Funct. Mater.* **2020**, *30*, 2000664.
[22] B. Kaplan, G. A. Gehring, *J. Magn. Magn. Mater.* **1993**, *128*, 111.
[23] S. Jin, Y. Wang, H. Zheng, S. Dong, K. Han, Z. Wang, G. Wang, X. Jiang, X. Wang, J. Hong, H. Huang, Y. Zhang, T.-L. Xia, X. Wang, *Nano Lett.* **2024**, *24*, 5467.
[24] Y. Yafet, E. M. Gyorgy, *Phys. Rev. B.* **1988**, *38*, 9145.

[25] C. Zhang, C. Liu, S. Zhang, B. Zhou, C. Guan, Y. Ma, H. Algaidi, D. Zheng, Y. Li, X. He, J. Zhang, P. Li, Z. Hou, G. Yin, K. Liu, Y. Peng, X. X. Zhang, *Adv. Mater.* **2022**, *34*, 2204163.
[26] A. Castellanos-Gomez, M. Buscema, R. Molenaar, V. Singh, L. Janssen, H. S. J. van der Zant, G. A. Steele, *2D Mater.* **2014**, *1*, 011002.
[27] G. Zhang, J. Yu, H. Wu, L. Yang, W. Jin, W. Zhang, H. Chang, *Appl. Phys. Lett.* **2023**, *123*, 101901.
[28] K. Huang, D.-F. Shao, E. Y. Tsymbal, *Nano Lett.* **2022**, *22*, 3349.
[29] H. Yang, J. Liang, Q. Cui, *Nat. Rev. Phys.* **2022**, *5*, 43.
[30] a) J. B. Tai, Smalyukh I. I., *Phys. Rev. Lett.* **2018**, *121*, 187201; b) D. Foster, C. Kind, P. J. Ackerman, J.-S. B. Tai, M. R. Dennis, I. I. Smalyukh, *Nat. Phys.* **2019**, *15*, 655; c) A. K. Nayak, V. Kumar, T. Ma, P. Werner, E. Pippel, R. Sahoo, F. Damay, U. K. Rossler, C. Felser, S. S. P. Parkin, *Nature* **2017**, *548*, 561; d) H. Jani, J. C. Lin, J. Chen, J. Harrison, F. Maccherozzi, J. Schad, S. Prakash, C. B. Eom, A. Ariando, T. Venkatesan, P. G. Radaelli, *Nature* **2021**, *590*, 74; e) N. Kent, N. Reynolds, D. Raftrey, I. T. G. Campbell, S. Virasawmy, S. Dhuey, R. V. Chopdekar, A. Hierro-Rodriguez, A. Sorrentino, E. Pereiro, S. Ferrer, F. Hellman, P. Sutcliffe, P. Fischer, *Nat. Commun.* **2021**, *12*, 1562.
[31] a) A. Thiaville, S. Rohart, É. Jué, V. Cros, A. Fert, *EPL* **2012**, *100*, 57002; b) G. Chen, J. Zhu, A. Quesada, J. Li, A. T. N'Diaye, Y. Huo, T. P. Ma, Y. Chen, H. Y. Kwon, C. Won, Z. Q. Qiu, A. K. Schmid, Y. Z. Wu, *Phys. Rev. Lett.* **2013**, *110*, 177204; c) E. C. Stoner, E. P. Wohlfarth, *Philos. Trans. R. Soc. London, Ser. A: Math. Phys. Sci.* **1948**, *240*, 599.
[32] A. Vansteenkiste, J. Leliaert, M. Dvornik, M. Helsen, F. Garcia-Sanchez, B. Van Waeyenberge, *AIP Adv.* **2014**, *4*, 107133.
[33] a) H. Zhang, Y.-T. Shao, X. Chen, B. Zhang, T. Wang, F. Meng, K. Xu, P. Meisenheimer, X. Chen, X. Huang, P. Behera, S. Husain, T. Zhu, H. Pan, Y. Jia, N. Settineri, N. Giles-Donovan, Z. He, A. Scholl, A. N'Diaye, P. Shafer, A. Raja, C. Xu, L. W. Martin, M. F. Crommie, J. Yao, Z. Qiu, A. Majumdar, L. Bellaiche, D. A. Muller, et al., *Nat. Commun.* **2024**, *15*, 3828; b) C. Zhang, Z. Jiang, J. Jiang, W. He, J. Zhang, F. Hu, S. Zhao, D. Yang, Y. Liu, Y. Peng, H. Yang, H. Yang, *Nat. Commun.* **2024**, *15*, 4472; c) X. Lv, H. Lv, Y. Huang, R. Zhang, G. Qin, Y. Dong, M. Liu, K. Pei, G. Cao, J. Zhang, Y. Lai, R. Che, *Nat. Commun.* **2024**, *15*, 3278.
[34] G. Kresse, J. Furthmüller, *Phys. Rev. B.* **1996**, *54*, 11169.
[35] P. E. Blöchl, *Phys. Rev. B.* **1994**, *50*, 17953.
[36] J. P. Perdew, K. Burke, M. Ernzerhof, *Phys. Rev. Lett.* **1996**, *77*, 3865.
[37] V. I. Anisimov, F. Aryasetiawan, A. Lichtenstein, *J. Phys. C: Solid State Phys.* **1997**, *9*, 767.
[38] J.-E. Lee, S. Yan, S. Oh, J. Hwang, J. D. Denlinger, C. Hwang, H. Lei, S.-K. Mo, S. Y. Park, H. Ryu, *Nano Lett.* **2023**, *23*, 11526.
[39] J. Heyd, G. E. Scuseria, M. Ernzerhof, *J. Chem. Phys.* **2003**, *118*, 8207.
[40] H. J. Monkhorst, J. D. Pack, *Phys. Rev. B.* **1976**, *13*, 5188.
[41] D. Koelling, B. Harmon, *J. Phys. C: Solid State Phys.* **1977**, *10*, 3107.